

Article

Wind-Assisted Ship Propulsion of a Series 60 Ship Using a Static Kite Sail

Wayne Formosa ^{1,*}, Tonio Sant ¹ , Claire De Marco Muscat-Fenech ¹  and Massimo Figari ² 

¹ Department of Mechanical Engineering, Faculty of Engineering, University of Malta, MSD 2080 Msida, Malta

² Department of Electrical, Electronics and Telecommunication Engineering and Naval Architecture (DITEN), University of Genoa, 16145 Genoa, Italy

* Correspondence: wayne.formosa.17@um.edu.mt

Abstract: Following the International Maritime Organization's goal to reduce greenhouse gas emissions, the interest in the application of wind-assisted ship propulsion (WASP) in maritime transportation is on the rise. Although a variety of WASP systems exist, the application in maritime shipping is still limited, especially in the case of kite sails. This paper presents a numerical model to carry out a theoretical assessment of the influence of the kite planform area and wind speed on the aerodynamic performance of a kite sail providing propulsive assistance to a 75 m long ship having a Series 60 hull. A static kite sail is assumed, on which a tail wind generates a thrust force to pull the vessel via a tether. While the mass of the kite is neglected, that of the tether is accounted for. A model is implemented for the tensioned tether having a catenary profile. The results generally show a positive correlation between the aerodynamic forces and the kite parameters. As expected, the output parameter values corresponding to the optimal angle of attack for a range of vessel speeds are also found to increase with an increasing relative wind speed. It is concluded that a static 320 m² kite sail would be sufficient to meet the entire propulsion requirements of the vessel under consideration under appropriate wind conditions.

Keywords: wind-assisted ship propulsion; static kite sail; leading edge inflatable kite; catenary tether; Series 60 ship; wind shear



Citation: Formosa, W.; Sant, T.; De Marco Muscat-Fenech, C.; Figari, M. Wind-Assisted Ship Propulsion of a Series 60 Ship Using a Static Kite Sail. *J. Mar. Sci. Eng.* **2023**, *11*, 117. <https://doi.org/10.3390/jmse11010117>

Academic Editors: Galih Bangga and Martin Otto Laver Hansen

Received: 19 November 2022

Revised: 28 December 2022

Accepted: 31 December 2022

Published: 5 January 2023



Copyright: © 2023 by the authors. Licensee MDPI, Basel, Switzerland. This article is an open access article distributed under the terms and conditions of the Creative Commons Attribution (CC BY) license (<https://creativecommons.org/licenses/by/4.0/>).

1. Introduction

Maritime freight shipping covers 80–90% of the global trade. Due to the high energy efficiency of ships and increasing capacity of waterborne transportation, the demand for freight shipping is expected to increase [1]. It is anticipated that this sector will account for 17% of the carbon emissions by the year 2050 [2]. In 2018, the International Maritime Organization initiated the strategy that by 2050, the greenhouse gas emissions must decrease by 50% compared to those in 2008 [3,4]. The strategy has led to new regulations and reignited the interest in wind-assisted ship propulsion (WASP). With WASP, the use of conventional power sources, and thus the demand for harmful fossil fuels, will be reduced [5]. WASP systems can also be combined with alternative fuels or slow steaming, in which a ship travels at a reduced speed to make the most out of the available wind with the lowest ship resistance possible. The reduction in CO₂ emissions by slow steaming was investigated for a typical sailing route of a container ship in the Mediterranean Sea by Degiuli et al. [6]. For engines powered by low sulphur marine gas oil and liquefied natural gas, the reductions in CO₂ emissions can reach 286 t and 448 t, respectively.

WASP systems include traditional sails, rotor sails, kite sails, rigid sails and suction wings. Despite the existing variety, the widespread implementation of these WASP systems in the maritime shipping sector is still lacking. The lack in implementation is partly due to the high capital costs required paired with the uncertainty in the fuel consumption reduction rates achieved and the time required to make a significant environmental and economic impact [5]. A secondary data review analysis on the aforementioned WASP

systems is provided by Chou et al. [5]. According to Chou, rotor sails, kite sails and rigid sails have the greatest potential in WASP, with the rotor and kite sails reaching efficiencies of up to 50% and the rigid sails reaching 60%. In a study by Traut et al. [7], wind data for five trade routes were used to compare the wind power contribution of a kite sail and a rotor sail for true wind angles of up to 360° from the direction of the ship. The dynamic kite sail is considered to follow circular trajectories and the tether is assumed straight, with the mass assumed negligible for both. Traut [7] concluded that the power outputs for the kite sail are more volatile but can be higher than those for the rotor sail, which exploits the Magnus effect to generate the propulsive force. Whereas a crosswind is ideal for the rotor sail, the kite sail is found to work well in the case of a tail wind. The latter was also concluded by Leloup et al. [8] in a study comparing the sailing performance of a classical rig and a kite following a zero-mass model, which neglects the mass and sagging of the tether. In addition to this comparison, Leloup et al. [8] also compared different flight trajectories of a dynamic kite to the flight of a static kite and concluded that vertical and horizontal dynamic flights following a figure of eight trajectory are optimal for the upwind and downwind cases, respectively. Nonetheless, the benefit of a static kite sail for small wind angles is also highlighted, especially when considering the stability of the ship and relative ease of operation. In another study considering a merchant ship, Leloup et al. [9] investigated the fuel savings that can be achieved by auxiliary propulsion from both a static and a dynamic kite sail. It is concluded that a static kite sail is better than a dynamic kite sail for true wind angles of up to 50° from the ship direction. For true wind speeds of 9.77 m/s and 15.68 m/s, optimal operation of a 320 m² kite sail is found to be capable of reducing the fuel consumption of the 50,000 dwt British Bombardier tanker by 10% and more than 50%, respectively. However, the zero-mass model is again used such that the weight of the tether is neglected and the tether is assumed straight. The zero-mass model was also implemented by Bigi et al. [10] in a study investigating the dynamic coupling of a ship and a kite sail for auxiliary propulsion. Apart from concluding that the roll motion of a ship assisted by a kite sail can be lower than the roll motion of a ship that is not, Bigi et al. [10] suggested that the effect of the tether can be significant on the interaction of the kite sail with the ship. Thus, the need for a more accurate representation of the tether is highlighted. Existing literature works making use of the zero-mass model generally consider fixed lift-to-drag ratios for the kites and fixed lengths as inputs for the straight tether. In such cases, the equilibrium condition is satisfied when the resultant aerodynamic force on the kite is collinear to the straight tether and the wind power captured by the kite sail is limited by the input tether length.

When compared to other WASP systems, kite sails are capable of operating at higher altitudes within the atmospheric boundary layer, thus benefitting from larger wind speeds. Additionally, kite sails require relatively minimal deck space as the kite sail flies in front of the ship and only requires a mast at the foredeck for launch and recovery [7]. In fact, kite sails can be easily retrofitted to existing ships. Notwithstanding these benefits, kite sails still have a relatively low technology readiness level [11]. A commercially available fully automated dynamic kite sail system for WASP is provided by SkySails Yacht GmbH. SkySails provide kite sails with areas reaching 400 m² and capable of delivering up to 2 MW of propulsive power while operating at altitudes ranging from 100 m to 300 m [12]. In application for pumping kite generators, kites can even reach 600 m altitudes [13]. By following a figure of eight, the kite sail developed by SkySails is capable of generating as much as 25 times the power per square metre of sail area of conventional sails [14]. The dynamic kite sails developed by SkySails have also been retrofitted on the Beaufort and Beluga SkySails ships. The former is a 55 m long testing ship equipped with an 80 m² kite sail able to save up to 1200 litre of fuel daily [15] while the latter is 132 m long with a 160 m² kite sail that can reduce fuel consumption by 20% [16,17].

The manoeuvres performed by dynamic kites allow the capture of wind at a range of angles of the relative wind. On the other hand, static kite sails are simpler to control [8]. Hence, this study focuses on a static leading edge inflatable kite sail in the ideal scenario of

a horizontal tail wind with a speed greater than that of the ship to generate the drag that acts as the propulsive force. The analysis in this study considers a 75 m long ship having a Series 60 hull. The objective of this study is to use numerical modelling to investigate the performance and achievable power outputs of a kite sail in a WASP application. The effects of wind shear are taken into consideration. Unlike existing works which considered the tether as a straight line of fixed lengths, the computationally efficient model presented in this paper also aims to address the consideration of weight and sagging of the tether by considering the tether as a catenary cable that can be winched as necessary, based on the kite elevation required for static operation. Given that the tether lengths required in operation are expected to be considerable, the tether weight will have a substantial influence on the elevation of the kite and its aerodynamic performance when operating within the atmospheric boundary layer. In the model presented in this paper, a considerable weight per unit tether length will constrain a kite sail of a given area to operate at a lower elevation because less tether length is required to balance a given lift force. The formulated model enables the determination of the values to which the operational parameters have to be set in any given operating conditions. Therefore, it can be used to determine the performance characteristics of a kite sail for specific sailing routes. The model also has the potential to serve as the framework of a dynamic kite sail model. Hence, the paper serves the purpose of providing a computationally efficient model for modelling the contribution of thrust of a static kite sail for reducing the carbon footprint. The aim is to reduce the aforementioned uncertainty in the contribution to ship propulsion by a kite sail and thus increase the readiness level of the technology that has the potential of being another means of reaching the International Maritime Organization's goal to reduce carbon emissions.

The paper is organised as follows. Section 2 outlines the theory behind the numerical model. Equations for determining the resistance of a Series 60 ship, the wind profile within the atmospheric boundary layer, the aerodynamic forces that act on a kite sail, together with the profile of a tether under the action of its weight and the forces acting on the tether are provided. Section 2 also presents the equilibrium analysis of the kite system. The numerical model that was developed in Python using the equations provided in Section 2 is described in Section 3. Hence, Section 3 specifies the inputs of the model as well as how the model determines the elevation of the static kite sail studied in this paper for the given inputs through an iteration. The determination of the kite elevation satisfying the condition of static operation enables the calculation of the kite system parameters that lead to the determined elevation and the corresponding aerodynamic performance. Section 4 then presents the formulation of a parametric analysis to investigate the effects of the kite planform area and wind speed. Section 4 is followed by the presentation of the results and conclusions in Sections 5 and 6, respectively.

2. Background Theory

2.1. Modelling the Ship Resistance

Determining the resistance of a ship is essential to be able to model the characteristics of a WASP system. The categories of the ship powering problem important for such a case are the estimation of the effective power necessary to tow the ship at a given speed in calm water and the appropriate power margins to account for roughness, fouling and harsh weather. The effective power is the power that overcomes the main hull naked resistance as well as the appendage and air resistances [18].

The main hull naked resistance for the Series 60 single screw vessel can be estimated using Sabit's [19] regression analysis for the Series 60 Standard Series data. The hull parameters covered by this series are given in terms of the block coefficient C_B , length L , beam B , draught T and longitudinal centre of buoyancy LCB . A ship is considered a Series 60 vessel if the criteria $0.60 \leq C_B \leq 0.80$, $2.5 \leq B/T \leq 3.5$, $5.5 \leq L/B \leq 8.5$, and

$-2.5\%L \leq LCB \leq +3.5\%L$ from amidship are satisfied [20]. The optimum value of LCB varies with C_B . For a single screw vessel, it can be found using [21]:

$$LCB = 20(C_B - 0.675) \tag{1}$$

The speed range covered by Sabit’s [19] regression analysis is given in terms of the ship speed, V_k (kn), and the length, L_f (ft). The values of $V_k/\sqrt{L_f}$ considered range from 0.50 to 0.90 in increments of 0.05. The regression equation and the coefficients used in the equation together with the full procedure to estimate the naked resistance are given by Molland et al. [20]. After applying the skin friction correction for the specific length of the ship, the naked effective power in kilowatts is found from:

$$P_E = \frac{\odot_s \Delta^{\frac{2}{3}} V_k^3}{579.8} \tag{2}$$

with \odot_s and Δ being the corrected resistance coefficient and load displacement, respectively. For a ship shorter than 400 ft (122 m), the ship correlation factor is unity. The corresponding naked hull resistance for a given ship speed, V , is then given by:

$$R_{Naked} = \frac{P_E}{V} \times 1000 \tag{3}$$

Molland et al. [22] provide equations for the appendage and air resistances, R_{App} and R_{air} . However, sizing the appendages and deck structures is beyond the scope of this study. Molland et al. [22] state a maximum R_{App} of 5% of R_{Naked} for a single screw vessel while the air resistance can be 4% of the effective resistance, R_{Eff} [23]. For preliminary estimates, Molland et al. [22] approximate the power margin to 25% of the total power. Hence, the resistance, R_{PM} , due to this margin equates to a third of R_{Eff} . The total resistance is then found by the addition of the different components, derived to:

$$R_T = \left(\frac{35}{24}\right) \times R_{Naked} \tag{4}$$

2.2. Modelling the Wind Profile

Given that the atmospheric boundary layer extends to a few hundred metres above sea level, wind shear affects the performance of kite sails. Whereas less wind power is available at lower elevations, extreme tether tensions may be reached if the elevation is too high. The study presented here models the wind profile in accordance with the Logarithmic Law Profile as it extrapolates the free stream wind speed at a given elevation, z , from a known value at a reference height, z_{ref} , as a function the surface roughness length, z_0 . The approximate value of z_0 is 0.2 mm for calm open sea conditions and 0.5 mm for a blown sea [24].

For a moving vessel, the aerodynamic force at any elevation is determined by the relative wind speed at that elevation. The study only considers the case in which the ship travels at a speed V in the same direction as the wind. A paramount requirement for the kite sail to be able to propel the ship is that V is smaller than the wind speed at the kite elevation, $U_{z,k}$. Hence, the relative wind speed at a given elevation is given by [24]:

$$W_z = U_{z,ref} \frac{\ln\left(\frac{z}{z_0}\right)}{\ln\left(\frac{z_{ref}}{z_0}\right)} - V \tag{5}$$

Depending on the operating conditions, W_z at low elevations may be zero, below which

it will be negative. The elevation at which $W_z = 0$ m/s can be found using Equation (5). Denoting this elevation by z_s , the equation takes the form of:

$$z_s = z_0 e^{\frac{V}{U_{z,ref}} \ln\left(\frac{z_{ref}}{z_0}\right)} \tag{6}$$

2.3. Fundamental Wing Theory for Modelling the Aerodynamic Lift and Drag on a Kite

The cross-section of a leading edge inflatable kite sail can be approximated to an aerofoil. The lift, drag and pitching moment of an aerofoil are characterised by dimensionless section coefficients, c_l , c_d and c_m , which are functions of the angle of attack, α , and the Reynolds Number. An aerofoil reaches fully stalled conditions as α is increased to a critical value depending on the aerofoil shape [24,25]. Under real operating conditions involving intermittent wind, the kite encounters a time varying angle of attack. The latter induces unsteady aerodynamic phenomena such as dynamic stall, resulting in lift and drag coefficients to deviate considerably from those experienced for a steady angle of attack. Various models have been developed over the recent decades to cater for dynamic stall encountered by aircraft wings, as well as helicopter and wind turbine rotors. Examples include the first-order compressible and incompressible Beddoes–Leishman models [26,27], the second-order model by Bangga et al. [28] and the second-order Snel model [29] that account for unsteady aerodynamic effects. However, the present study assumes a static kite sail operating in a steady wind flow; thus, the influences of unsteady aerodynamics are not considered.

The resultant aerodynamic forces and moment of the distributed loads along the surface of an aerofoil can be assumed to act at any point along the chord line of the aerofoil as long as the value of the moment considered is correct for that same point. At the centre of pressure (COP), the effect of the moment is replicated by the resultant forces such that c_m takes a value of zero. A thin symmetrical aerofoil is assumed in this study, for which the COP is located at the quarter-chord from the leading edge. A symmetrical aerofoil is chosen over a cambered aerofoil for conservativeness since cambered aerofoils generally have higher lift coefficients than the symmetrical counterpart [25]. Although higher lift forces are expected to increase the kite elevation and enable the kite to generate a greater thrust due to the positive wind shear, the increased elevations may exceed reasonable limits.

The kite sail is considered to approximate a flat wing. The applicability of this assumption for curved kites needs to be studied using Computational Fluid Dynamics (CFD). Whereas the flow over an aerofoil is two-dimensional, the air in the case of a finite wing also flows in the spanwise direction. The requirement for the pressure difference between the upper and lower surfaces of the aerofoil to cease at the wing tips leads to a spanwise pressure gradient. Given the higher pressure on the lower surface, the flow over the latter is forced towards each tip while the opposite happens for the upper surface, creating tip vortices which induce downwash. Downwash alters the effective angle of attack and thus reduces lift and induces more drag, which is beneficial to a drag-driven kite sail [30]. One method to account for this downwash is to apply aspect ratio corrections to the section coefficients. According to the Lanchester–Prandtl Lifting Line Theory, an elliptical lift distribution leads to constant downwash that results in minimum induced drag. Hence, an elliptical planform area with an elliptical loading will be assumed with the aim of being conservative. The Lifting Line Theory gives the lift coefficient for a finite wing with a given aspect ratio, AR , as [31]:

$$C_L = \frac{c_l}{1 + \frac{c_l}{\pi \cdot AR}} \tag{7}$$

The theory also provides an equation for the induced drag coefficient, $C_{D,i}$, for small angles of attack. For high angles of attack, this equation can be modified to [31]:

$$C_{D,i} = C_L \tan\left(\frac{C_L}{\pi \cdot AR}\right) \tag{8}$$

The overall drag coefficient is then found from [31]:

$$C_D = c_d + C_{D,i} \tag{9}$$

Hence, the kite lift for a relative wind speed, $W_{z,k}$, at the kite elevation is given by:

$$L_k = \frac{1}{2} C_L \rho_a A_k W_{z,k}^2 \tag{10}$$

while the drag can be found from:

$$D_k = \frac{1}{2} C_D \rho_a A_k W_{z,k}^2 \tag{11}$$

where ρ_a is the air density and A_k is the planform area of the kite having an elliptical profile.

2.4. Modelling the Catenary Tether of a Kite

In WASP, the tether is the means of connection and force translation between the kite and the ship. Meriam et al. [32] derived the static analysis of a flexible tether, which is sufficient for the purpose of this work since the static kite system is analysed from a quasistatic perspective. The static analysis neglects any resistance of the tether to bending such that the vector of the tension at any point along the tether is tangential to the tether at that same point. The static analysis also highlights the fact that the horizontal component of the tether tension, T_H , remains constant throughout the whole span of the tether and that the vertical component diminishes to zero at the connection point to the ship such that the tension at the connection point consists only of the horizontal counterpart. As a result, the tether at this point is perfectly horizontal.

In this work, a uniform inelastic tether is implemented such that elongation and deformation are neglected. The effect of the drag on the tether resulting from the relative wind speed on the performance of the kite system is also neglected. As already explained, the only scenario being considered in this study is that in which the relative wind speed is in the forward direction of the ship. While the horizontal components of any tether drag would effectively contribute towards propulsion, the downward components on the sloping tether would result in a lower kite elevation and thus, lead to a decrease in the kite thrust as a result of the decrease in the relative wind speed due to wind shear. Effectively, the adopted approach assumes that the tension along the tether in equilibrium is a result of its own weight only such that the tether takes a catenary shape [32].

The connection point at the ship is considered as the origin for the tether end coordinates. Meriam et al. [32] show the vertical coordinate or elevation for a catenary tether with a weight per unit length μ_t and a horizontal coordinate x_t to be given by [32]:

$$z_t = \frac{T_H}{\mu_t} \left(\cosh \frac{\mu_t x_t}{T_H} - 1 \right) \tag{12}$$

The tether length, l_t , is found using [32]:

$$l_t = \frac{T_H}{\mu_t} \sinh \frac{\mu_t x_t}{T_H} \tag{13}$$

From the above equation, the horizontal coordinate, x_t , for a given vertical tension component, T_V , at the tether end can be derived as [32]:

$$x_t = \frac{T_H}{\mu_t} \sinh^{-1} \left(\frac{T_V}{T_H} \right) \tag{14}$$

The tether tension, T_t , at the tether end is equivalent to the resultant of T_H and T_V , and can be calculated as a function of the elevation of the latter using [32]:

$$T_t = T_H + \mu_t z_t \tag{15}$$

Given that the tether in this work is assumed inelastic and the kite system analysis is quasistatic, the stiffness matrix to account for fluctuating loads can be neglected.

To analyse the significance of the tether drag, it can be estimated by treating the tether as a column and calculating the drag in the forward direction only. Assuming a constant ρ_a , the only parameter that varies with elevation for a tether of constant diameter, d_t , is the relative wind speed. Hence, the drag on the tether can be found using integration from:

$$D_t = \frac{1}{2} C_{D,t} \rho_a d_t \int_{z_s}^{z_t} \left[U_{z,ref} \frac{\ln\left(\frac{z}{z_0}\right)}{\ln\left(\frac{z_{ref}}{z_0}\right)} \right]^2 - 2V \left[U_{z,ref} \frac{\ln\left(\frac{z}{z_0}\right)}{\ln\left(\frac{z_{ref}}{z_0}\right)} \right] + V^2 dz \tag{16}$$

The length-to-diameter ratio of each infinitesimal element will be assumed infinite given the adjacent elements, for which White [33] suggests a tether drag coefficient, $C_{D,t}$, of 1.20.

2.5. Equilibrium Analysis of the Kite-Tether Assembly

The kite system configuration following the theory is illustrated in Figure 1, with the aerodynamic forces acting at the quarter-chord due to the assumption of a thin symmetrical aerofoil. The length Δz is the vertical distance between the quarter-chord or COP of the kite and the tether end. Given the approximation of the kite sail to a flat wing, the aerofoil shown in Figure 1 represents the midspan aerofoil of the elliptical planform assumed for this study. Although a kite mass would expectedly result in lower elevations and hence lower thrust forces due to wind shear, Figure 1 considers the weight of the kite to be negligible compared to the aerodynamic forces and tether weight. The point O represents the connection point to the ship. Neglecting the mast used to hoist the kite and the freeboard of the ship, the horizontal plane at O is treated as the mean sea water level. The kite sail is connected to the catenary tether by means of bridle lines. Whereas each set of bridle lines would, in practice, consist of multiple lines distributed along the curved span of the kite, this study only considers one front bridle line connected to the leading edge of the kite and a rear one connected to the trailing edge. For a given elevation, z_k , of the kite’s COP, equilibrium about the tether end requires the horizontal coordinate of the kite’s COP to satisfy Equation (17). The equation was derived by taking moments of the lift and drag about the tether end where the bridle lines are connected.

$$x_k = \frac{D_k \Delta z}{L_k} + x_t \tag{17}$$

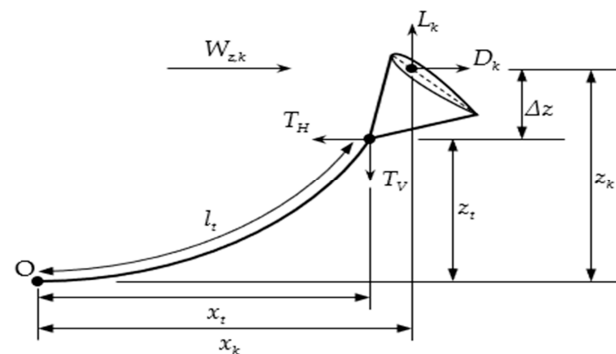


Figure 1. A two-dimensional representation of the kite system configuration and external forces for the ideal case that the wind and ship direction are the same for a forward relative wind speed, $W_{z,k}$.

Figure 2 depicts the geometry of the bridle lines system and the forces acting on it, including the internal forces. The aerofoil chord in the plane shown is that at the midspan of the elliptical planform and it is referred to as the reference chord, c_{ref} . The equilibrium analysis of Figure 2 leads to Equations (18) and (19) for the horizontal and vertical force components, as well as to the conclusion that $D_k = T_H$ and $L_k = T_V$.

$$D_k = T_r \cos \beta + T_f \cos \zeta \tag{18}$$

$$L_k = T_r \sin \beta + T_f \sin \zeta \tag{19}$$

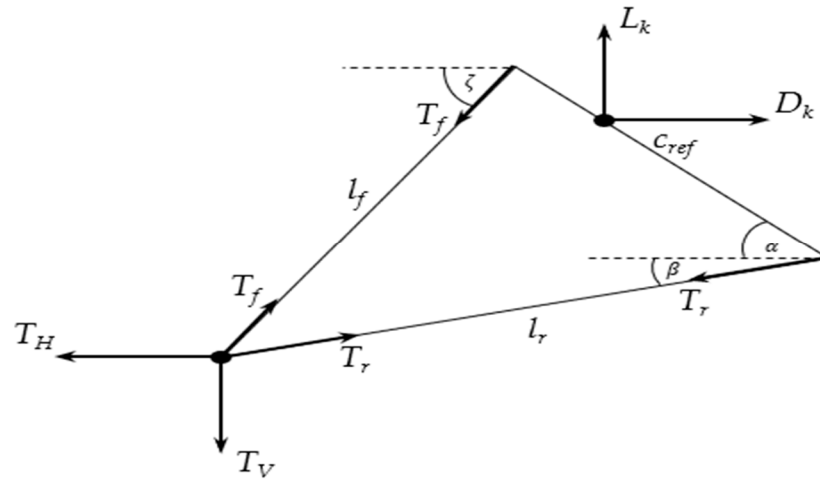


Figure 2. A free body diagram of the bridle lines of the kite sail showing the geometry together with the external and internal forces acting in equilibrium conditions for a given angle of attack, α .

For a given angle of attack, α , the length, l_f , of the front bridle line is found geometrically from:

$$l_f = \sqrt{(x_k - x_t - 0.25c_{ref} \cos \alpha)^2 + (\Delta z + 0.25c_{ref} \sin \alpha)^2} \tag{20}$$

while length, l_r , of the rear bridle line is given by:

$$l_r = \sqrt{(x_k - x_t + 0.75c_{ref} \cos \alpha)^2 + (\Delta z - 0.75c_{ref} \sin \alpha)^2} \tag{21}$$

The angles β and ζ defined in Figure 2 can then be found from the tangent formula. A positive value for ζ can be ensured by use of the CAST Rule. From Equations (18) and (19), the tension in the front bridle line, T_f , is given in terms of β and ζ by:

$$T_f = \frac{L_k - D_k \tan \beta}{\sin \zeta - \cos \zeta \tan \beta} \tag{22}$$

whereas the tension in the rear bridle line, T_r , can then be calculated from:

$$T_r = \frac{D_k - T_f \cos \zeta}{\cos \beta} \tag{23}$$

3. Numerical Model

The numerical model adopted for this study was developed using Python 3.9.12. The model is based on the configuration illustrated in Figures 1 and 2 for equilibrium conditions with use of the discussed theory. A simplified flowchart of the algorithm followed is provided in Figure 3.

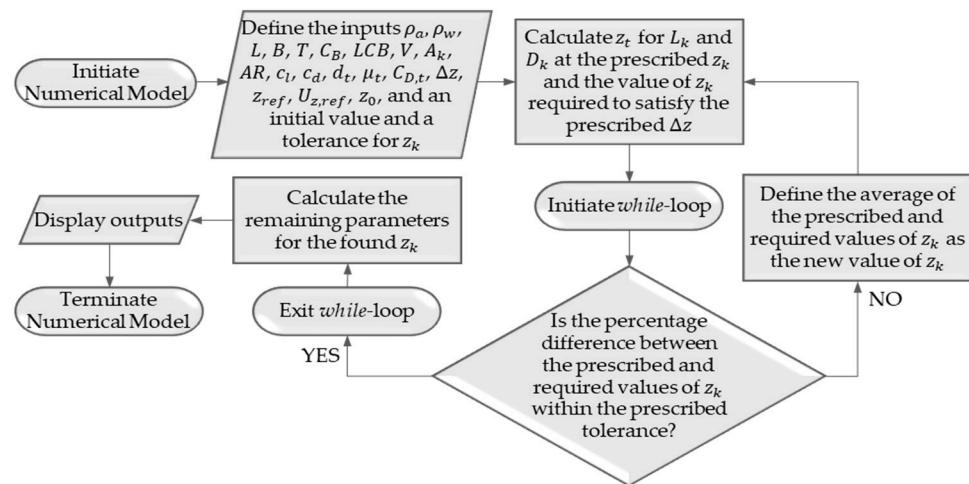


Figure 3. A flow chart explaining the main steps of the algorithm adopted for the numerical model.

The inputs include the air and water properties such as the densities ρ_a and ρ_w , as well as the ship, kite, tether and wind parameters. The ship parameters required for this study are the length, beam, draught, block coefficient, LCB as found using Equation (1), and V . Assuming negligible kite mass, the kite parameters are the kite area, A_k , for an elliptical planform, AR , an initial value for z_k as well as c_l and c_d for the range of α considered. The tether parameters are d_t , μ_t and $C_{D,t}$. Another input is the vertical distance, Δz , between the tether end and the kite’s quarter-chord, as defined in Figure 1. The Δz input is of paramount importance to this study as it is the parameter used to iterate z_k and hence assure a configuration similar to that depicted in Figure 1. Given the use of the Logarithmic Law to model the wind, the parameters for the latter are z_{ref} , $U_{z,ref}$ and z_0 .

The iteration performed by means of the *while*-loop illustrated in Figure 3 involves calculating $W_{z,k}$, L_k , D_k , x_t and z_t using Equations (5), (10)–(12) and (14), respectively. Therefore, C_L and C_D need to be calculated using Equations (7) and (9). The value of z_k required for the prescribed Δz and calculated z_t together with the percentage difference between the prescribed z_k and the required z_k are also necessary to perform the iteration. Once the tolerance prescribed for the percentage difference between the prescribed z_k and the required z_k is satisfied, the parameters calculated in the *while*-loop are assigned with the respective values and the remaining parameters are calculated. The outputs useful for analysing the performance of the kite sail are the ship resistance, the coordinates of the COP of the kite, the aerodynamic forces on the kite, the lengths and tensions of the bridle lines and tether as well as the tether drag. While z_k is found from the iteration, the value of x_k necessary for equilibrium about the tether end is calculated using Equation (17). Since D_k is effectively the propulsive force of the kite sail, it can be used to find the propulsive force as a percentage of R_T found from Equation (4). The values for l_f , l_r and l_t are calculated using Equations (13), (20) and (21), whereas those for T_f , T_r and T_t are determined from Equations (15), (22) and (23). The tether drag is estimated as D_t in Equation (16) and output as a percentage of D_k .

4. Numerical Simulations

The numerical model algorithm is used to perform a parametric analysis with the aim of investigating the performance of the kite sail in application for WASP of a Series 60 ship. The NACA-0015 aerofoil, of which section coefficients for a range of α and Reynolds Numbers are provided by Sheldahl and Klimas [34], is chosen for the kite sail and assumed to be a thin symmetrical aerofoil. The ship parameters, given in Table 1, are derived from the midpoints of the Series 60 Standard Data criteria stated in Section 2.1 and a V_k of 11 knots. For the given value of L , the speed range with which the ship can travel while remaining within the criteria is from 4.04 to 7.23 m/s. The total ship resistance for each

ship speed within this range is illustrated in Figure 4. The naked hull resistance of this ship was validated using the MAXSURF Resistance software [35].

Table 1. The input parameters of the Series 60 ship adopted in this study.

Parameter	L (m)	B (m)	T (m)	C_B (-)	LCB (%L)
Value	75.23	10.75	3.58	0.70	0.50

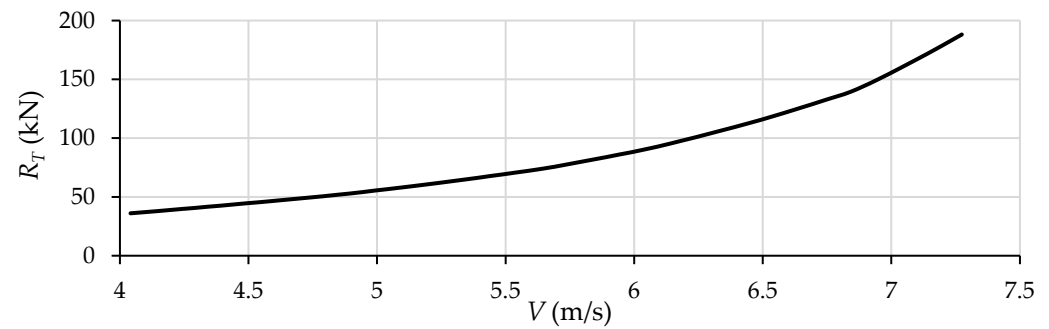


Figure 4. The resistance of the Series 60 ship considered in this study for the whole speed range.

The parameters investigated in this work are A_k and $U_{z,ref}$, with the analysis also combining the effect of α and V . Hence, the remaining inputs stated in Section 3 are considered as fixed parameters, including ρ_a and ρ_w , set to 1.08 kg/m^3 and 1025 kg/m^3 , respectively. Table 2 shows the values for the remaining fixed inputs. Given the likelihood of the kite to be operating in strong winds, z_0 is set to the value stated for a blown sea in Section 2.2. Although this study uses Δz to set the kite configuration, its effect is not investigated and thus, it is fixed to a value of 5 m. A high value of 10 is prescribed to AR of the finite wing to allow for the spanwise pressure gradient explained in Section 2.3. While $C_{D,t}$ was set as suggested by White [33] for an infinite length-to-diameter ratio, the values of d_t and μ_t were obtained through a separate tether analysis using the same numerical model and fixed parameter values. The tether analysis is explained in further detail below. Also determined from the tether analysis are the maximum A_k and $U_{z,ref}$ considered.

Table 2. The fixed input parameters adopted for the wind profile, kite sail and tether.

Parameter	z_{ref} (m)	z_0 (mm)	Δz (m)	AR (-)	d_t (mm)	μ	$C_{D,t}$ (-)
Value	90	0.5	5	10	42	64.8	1.2

The chosen tether is a bright wire rope made of improved plow steel with a fibre core. From the tether analysis, such a rope was found to have sufficient safe loads and a weight per unit length that generally results in kite elevations within the 600 m limit stated in Section 1 for the highest relative wind speed considered. The properties of different diameters of the wire rope are available in [36] and the aerofoil section coefficients of interest to this study are those for $1^\circ \leq \alpha \leq 90^\circ$ for a single Reynolds Number. For $30^\circ \leq \alpha \leq 90^\circ$, the coefficients at each value of α provided by Sheldahl and Klimas [34] are independent of the Reynolds Number. Hence, the tether analysis starts by first running the Python code for different tether diameters and then determining which diameters lead to a tether end tension that does not exceed the corresponding safe load. The tether analysis is carried out for $30^\circ \leq \alpha \leq 90^\circ$ only given that the Reynolds Number for the smaller angles of attack is not determined at this point. With the aim of accounting for the worst-case scenario, this step was carried out for $V = 0 \text{ m/s}$. After comparison of the different combinations of the tether diameters available in [36] as well as A_k and $U_{z,ref}$, a tether diameter of 42 mm with a safe load of 190 kN in conjunction with a maximum A_k and $U_{z,ref}$ of 320 m^2 and

20 m/s was considered reasonable. The maximum x_k and z_k observed for these values at $V = 4.04$ m/s are about 800 m and 420 m, with A_k and z_k within the limits from literature already discussed. For $\alpha < 30^\circ$, c_l and c_d were found through an iteration of the Reynolds Number until its value obtained for $\alpha < 30^\circ$ was approximately equal to the Reynolds Number to which the input coefficients correspond. The lift and drag section coefficients used for the NACA-0015 aerofoil for $1^\circ \leq \alpha \leq 90^\circ$ are plotted in Figures 5 and 6.

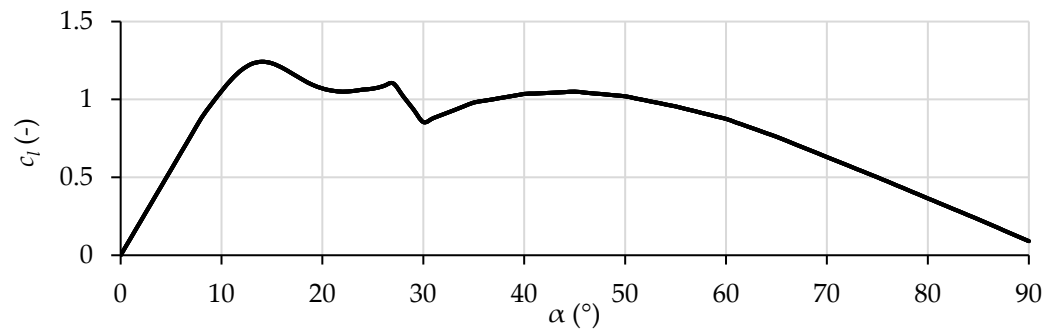


Figure 5. The lift coefficients of the NACA-0015 aerofoil, obtained by iterations of the average Reynolds Number for $\alpha < 30^\circ$ and independent of the Reynolds Number for $\alpha \geq 30^\circ$.

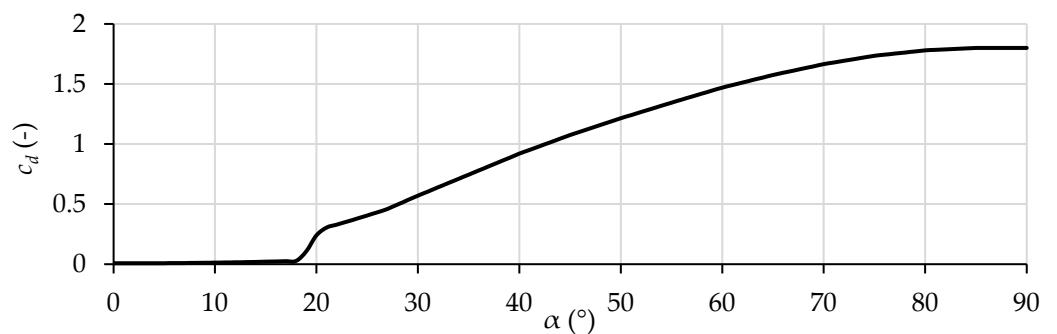


Figure 6. The drag coefficients of the NACA-0015 aerofoil, obtained by iterations of the average Reynolds Number for $\alpha < 30^\circ$ and independent of the Reynolds Number for $\alpha \geq 30^\circ$.

Once all the values of the fixed input parameters together with the maximum A_k and $U_{z,ref}$ were determined, the parametric analysis was carried out. Given the value of 320 m^2 determined for the maximum A_k , the values considered in the parametric analysis for A_k are of 40 m^2 , 80 m^2 , 160 m^2 and 320 m^2 to study the effect of doubling the kite area. The corresponding values of c_{ref} are 2.55, 3.60, 5.09 and 7.20 m, while those of the span are 20.00, 28.28, 40.00 and 56.57 m. On the other hand, the values for $U_{z,ref}$ are of 10 m/s, 15 m/s and 20 m/s given the maximum value determined from the tether analysis. The reason behind the lower limit of 10 m/s is to ensure a positive relative wind speed for the maximum ship speed of 7.27 m/s determined from the Series 60 Standard Data criteria. The whole speed range determined from the Series 60 Standard Data criteria was considered by repeating each combination for 4.04, 4.85, 5.66, 6.47 and 7.27 m/s, equivalent to 7.85, 9.43, 11.00, 12.58 and 14.13 kn. For the analyses of A_k and $U_{z,ref}$, $U_{z,ref}$ and A_k were set to the corresponding maximum value of 20 m/s and 320 m^2 , respectively, to investigate the greatest potential of each of the two parameters. A single run of the Python code explained in Figure 3 generates results for a single V and $1^\circ \leq \alpha \leq 90^\circ$ with an average computational time of only around 661 ms with an Intel® Core™ i7-8750H processor.

5. Results and Discussion

This section presents and discusses the results generated from the parametric analysis outlined in Section 4. In this study, the performance of the kite for WASP applications is characterised by the kite coordinates, the aerodynamic forces acting on the kite and the

achieved propulsion as a percentage of the ship resistance, together with the corresponding lengths and tensions of the bridle lines and tether. The results first highlight the influence of the kite area along with the angle of attack on the coordinates and aerodynamic forces of the kite as well as the lengths and tensions of the bridle lines. Then, the variation in the optimal values of the parameters at different ship and reference wind speeds is analysed. The parameters investigated in the wind speed study are the optimal angle of attack that leads to the maximum kite thrust and the corresponding the kite coordinates, propulsion assistance, and the length and tensions of the tether. The tether drag as estimated in this study is also analysed. Each set of coordinates presented satisfies the condition $\Delta z \approx 5$ m prescribed in Section 4 with a tolerance of 0.1% and assures quasistatic equilibrium about the tether end. Equilibrium between the kite system and the vessel is not considered as a mandatory requirement as it is being assumed that the remainder of the ship resistance for cases in which the percentage assistance from the kite sail is less than 100% is provided through propeller-type propulsion systems. On the other hand, percentages greater than 100% mean that the kite thrust is higher than the ship resistance such that the vessel would accelerate. Such cases imply that the vessel is capable of travelling at a higher speed while still only relying on the kite sail for propulsion.

5.1. Investigating the Influence of the Kite Area

The kite area study involves the variation of A_k from 40 to 320 m² with all the other variables kept constant, including the reference wind speed, $U_{z,ref}$, set to 20 m/s. The plots in this section are those for the highest vessel speed of 7.27 m/s, for which the relative wind speed at the kite elevation, $W_{z,k}$, will be the lowest but the ship resistance is the largest. A high vessel speed is often desirable to minimise the voyage time. Hence, these plots will serve to determine the variation in the parameters corresponding to the minimum possible assistance in ship propulsion by a kite sail.

Figure 7 shows how the elevation of the kite, z_k , varies with α , and the kite area, A_k . The graph immediately indicates that A_k is a major contributor to the elevation at which the kite has to be flown, mainly due to the direct proportionality between the aerodynamic forces and A_k as established in Equations (10) and (11). For V equal to 7.27 m/s, z_k increases steadily to a maximum of 59.8 m, 141.9 m, 341.0 m and 812.2 m for A_k values from 40 to 320 m² at an angle of attack 14°. Beyond $\alpha = 30^\circ$, another peak, but with a much smaller magnitude, is present at the α of around 35°. The corresponding z_k values as A_k is increased from 40 to 320 m² are 21.1 m, 45.5 m, 106.8 m and 256.4 m. Hence, these values indicate that doubling the kite area increases z_k by around 140% at an α of 14° and around 130% at 35°. As α approaches 90°, z_k diminishes to about 5 m for all kite areas. The main contributing factor to this value is the prescription of 5 m to Δz since, despite never reaching zero, the elevation of the tether end, z_t , at this α is very low. In relation to the kite area, the convergence to 5 m means that the effect of A_k also diminishes as α tends to 90°.

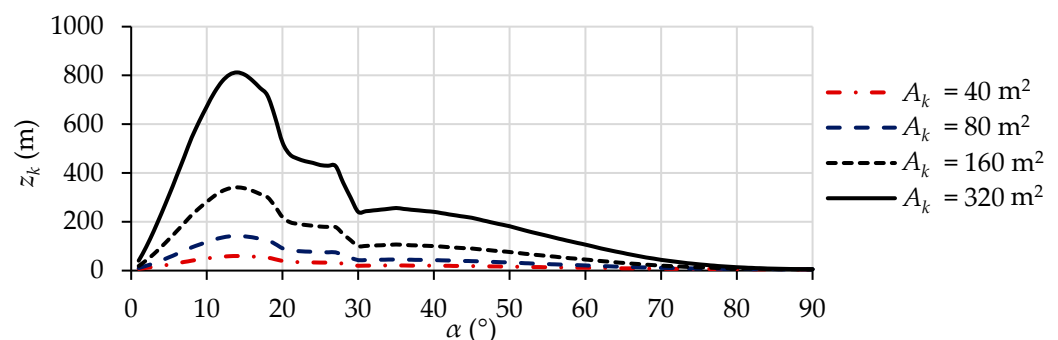


Figure 7. The kite elevations for each kite area and angle of attack at a ship speed of 7.27 m/s and a reference wind speed of 20 m/s.

The coordinates, x_k , of the kite's COP required for equilibrium conditions at each of the corresponding values of z_k in Figure 7 are given in Figure 8. For the same reason explained for z_k , x_k is greatly dependent on the kite area. Comparing x_k and z_k shows dissimilar trends for the dependency on α . The maximum x_k is not reached at $\alpha = 14^\circ$, indicating that a high z_k does not necessarily require a relatively high x_k for equilibrium. The results indicate that the average increases that have to be applied to x_k if A_k is doubled are of about 143% at 15° and 27° , about 140% at 30° and about 138% at 45° . Hence, the angle of attack of the kite within this range appears to have a relatively low significance on the effect of A_k when compared to the case of z_k . The peak at 45° corresponds to the maximum x_k that has to be reached for the 320 m^2 and 160 m^2 kite areas. At an α of 90° , x_k converges to approximately the same value for all four kite areas. Starting at 102.3 m for 40 m^2 , x_k has to be 2%, 4% and 7% higher for each consecutive A_k up to 320 m^2 . With the peak at $\alpha = 45^\circ$ for $A_k = 80 \text{ m}^2$ being equal to 83.5 m , the maximum value of x_k that has to be achieved for the smaller two areas is that at $\alpha = 90^\circ$. The reason behind the relatively small percentage difference at 90° could be the fact that z_k is approximately the same for all areas, thus indicating that the aerodynamic effects at this angle of attack have similar effects, irrespective of the area.

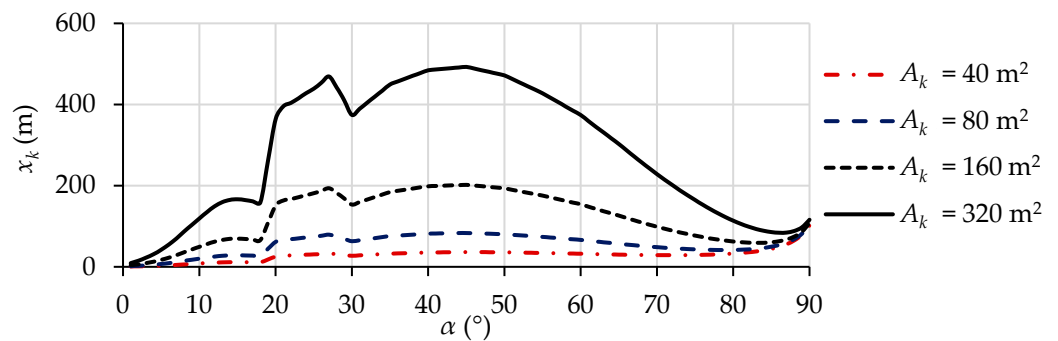


Figure 8. The kite horizontal coordinates for each kite area and angle of attack at a ship speed of 7.27 m/s and a reference wind speed of 20 m/s .

Figure 9 illustrates the variation in the lift forces, L_k , at the corresponding coordinates in Figures 7 and 8. The line graphs in Figure 9 have a similar shape to those for z_k in Figure 7. The similarity indicates that the kite elevation that has to be set for any given α and A_k for the lift acting on the kite sail to satisfy the condition $\Delta z \approx 5 \text{ m}$ is positively correlated to L_k . The correlation is due to the fact that, at higher elevations, higher aerodynamic forces are experienced by the kite in the presence of a positive wind shear. In turn, an increase in lift has to be accompanied by an increase in the kite elevation because a higher z_t is required for the tether weight to balance L_k . This requirement also explains the relationship which z_k and L_k have with A_k given the direct effect of the latter on L_k . In fact, considering the α value of 14° at which L_k is maximum, L_k for each consecutive area results as 150%, 145% and 140% higher than the value of L_k for the lower adjacent area as A_k is gradually doubled to 320 m^2 . These percentages indicate that the rates at which L_k and z_k increase with A_k are non-linear, with the rate decreasing for larger kite areas. For a particular α , using a kite sail twice the size at a given elevation doubles L_k which, in turn, calls for an increase in z_k . The increase in z_k is accompanied by a logarithmic increase in the relative wind speed, $W_{z,k}$, which affects L_k on a quadratic degree. The relationship discussed for z_k and L_k is also visible as the angle of attack reaches 90° since both experience a decline. As z_k at this α is approximately the same for each kite area, the lift is expected to be, in reality, only affected by A_k . In fact, L_k for a given area is about 100% higher than that for the next smaller area being considered.

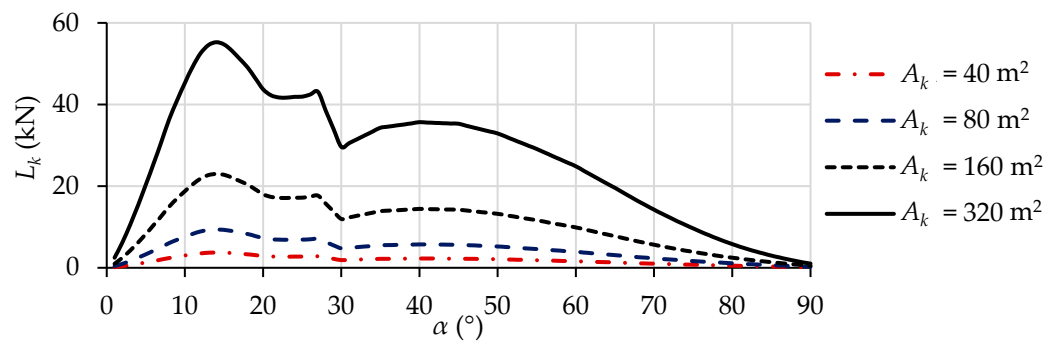


Figure 9. The kite lift forces for each kite area and angle of attack at a ship speed of 7.27 m/s and a reference wind speed of 20 m/s.

The graph for the drag, D_k , effectively being the propulsive force that is generated by this WASP system, is presented in Figure 10. Comparison of Figure 10 to Figures 7 and 8 indicates that the maximum propulsive force is not achieved at the highest z_k or x_k . At V equal to 7.27 m/s, it is achieved at $\alpha = 60^\circ$. The corresponding coordinates are (32.3 m, 11.6 m), (66.4 m, 21.0 m), (154.2 m, 45.5 m) and (374.2 m, 106.7 m) for the kite areas from 40 m² to 320 m². The propulsion at these points corresponds to 1.5%, 3.7%, 9.2% and 23.2%, respectively, of the resistance at $V = 7.27$ m/s, with an average increase of about 150% each time the kite is doubled in size. The increase can be attributed to the relationship with $W_{z,k}$ in the same manner discussed for L_k . Given that z_k and $W_{z,k}$ at $\alpha = 90^\circ$ vary only to a small degree for different kite areas, the propulsive force at this angle mainly depends on A_k . In fact, the increase seen in D_k each time the kite area is doubled is about 100%. The appendage resistance, R_{App} , air resistance, R_{Air} , and resistance due to the power margin, R_{PM} , contribute towards 3.4%, 3% and 25% of the total ship resistance, respectively, as labelled in Figure 10. Hence, a kite area of 80 m² is large enough to provide enough thrust to overcome R_{App} or R_{Air} , that of 160 m² exceeds the two resistances combined by a margin of 43%, while that of 320 m² can make up for most of R_{PM} .

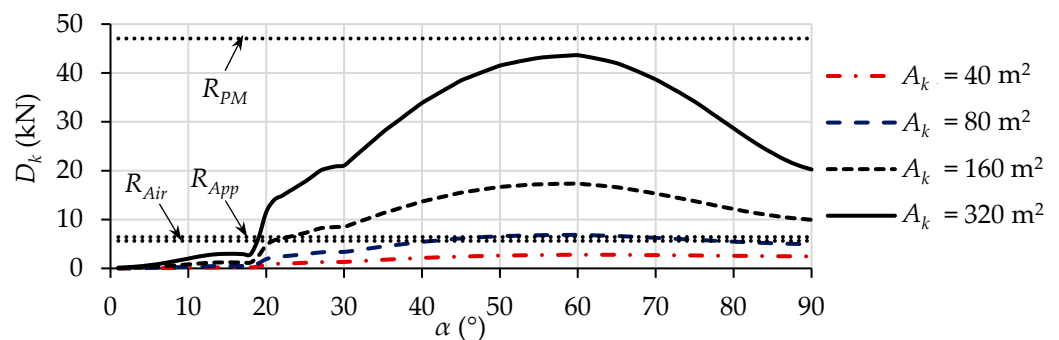


Figure 10. The kite thrust forces compared to the air resistance, appendage resistance and power margin of the Series 60 ship at a ship speed of 7.27 m/s and a reference wind speed of 20 m/s.

The lengths of the front and rear bridle lines vary with α similarly to each other, as shown in Figure 11. They are also influenced only marginally by the kite area. The different reference chords, c_{ref} , attributed to each area are a possible contribution to this. Starting from an average of 5.1 m and 6.3 m, l_f and l_r increase rapidly to about 100.5 m and 100.4 m, respectively, as α reaches 90°. The bridle line lengths do not necessarily increase with A_k . At an α of 10°, l_f for an area of 160 m² is only 1.0% higher than that for 80 m², while that for 80 m² is only 1.5% lower than the length at the area of 40 m². The rapid increase can be a consequence of the kite coordinates at high angles of attack. While z_k decreases to about 5 m, x_k is always greater than 100 m. Hence, the horizontal coordinate of the tether end is small such that the high values of x_k for equilibrium have to be reached by lengthening the

bridle lines. With an angle of attack of 60° , l_f and l_r need to be set to an average of 10.2 m and 10.8 m, respectively, for maximum thrust.

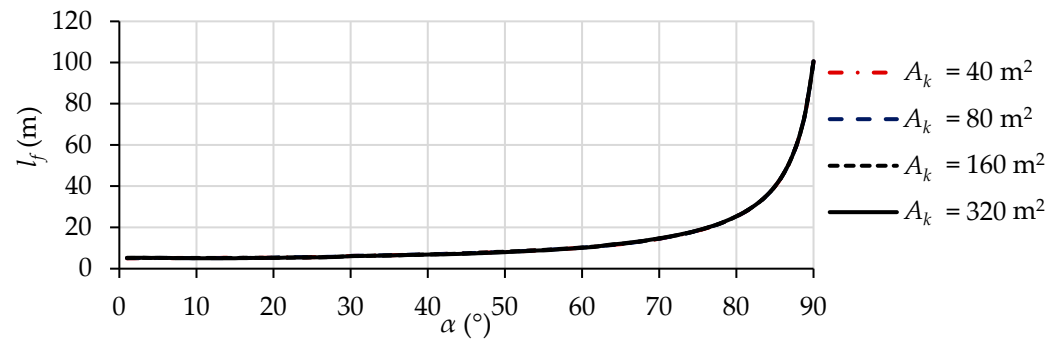


Figure 11. The front bridle line lengths for each kite area and angle of attack at a ship speed of 7.27 m/s and a reference wind speed of 20 m/s.

The tension in the front bridle line, T_f , and that in the rear bridle line, T_r , exhibit a significant difference from each other, mainly due to the COP of the kite being at the quarter-chord location. The variation in T_f is illustrated in Figure 12. Although T_f and T_r have similar relationships with α , that between the two is not consistent. The minimum percentage by which T_f is higher than T_r is of 109%, corresponding to $A_k = 320 \text{ m}^2$ and $\alpha = 1^\circ$, while the maximum is of 219%, corresponding to $A_k = 40 \text{ m}^2$ and $\alpha = 18^\circ$. The maximum tensions are experienced with $\alpha = 14^\circ$, with the values being equal to 2.9 kN, 7.4 kN, 18.7 kN and 47.8 kN for T_f , and equal to 0.9 kN, 2.5 kN, 6.7 kN and 19.9 kN for T_r . For α equal to 60° , the percentage increases in T_f are 145%, 153% and 154% starting from 2.4 kN for $A_k = 40 \text{ m}^2$, whereas the increases in T_r are 149%, 161% and 168%, starting from 0.8 kN. On the other hand, the values of T_f at $\alpha = 90^\circ$ are equal to 1.9 kN, 3.7 kN, 7.5 kN and 15.2 kN for kite areas varying between 40 m^2 and 320 m^2 , while the corresponding values of T_r are equal to 0.6 kN, 1.2 kN, 2.5 kN and 5.1 kN. The percentage increases of about 100% indicate that as α is increased to 90° , the bridle line tensions are mainly affected by the kite area. It is noted that, assuming that the bridle lines are of the same material and diameter of the tether, the safe load of 190 kN is never reached for the ship speed of 7.27 m/s.

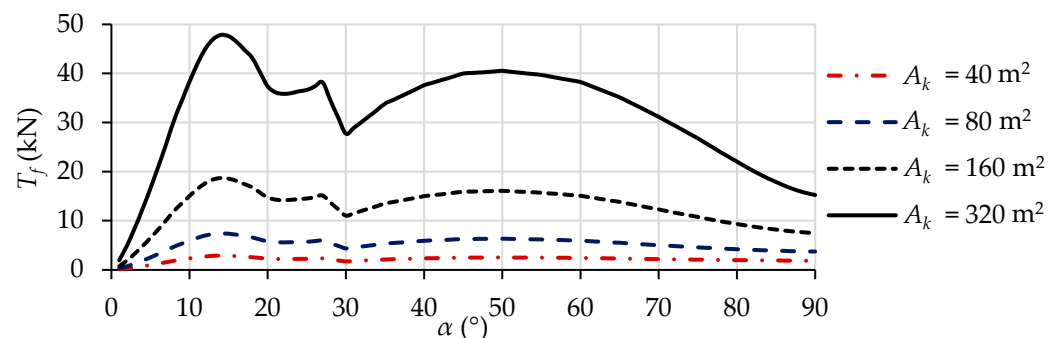


Figure 12. The front bridle line tensions for each kite area and angle of attack at a ship speed of 7.27 m/s and a reference wind speed of 20 m/s.

5.2. Investigating the Influence of the Wind Speed

For the wind speed study, the highest kite area of 320 m^2 was considered such that the greatest potential of the kite sail in different operating conditions is investigated. The different values considered for the reference wind speed, $U_{z,ref}$, are 10, 15 and 20 m/s. The variation in the different parameters with α follows similar trends as those discussed in Section 5.1. Hence, this section focuses on the optimal parameters for different wind and ship speeds. The optimal parameters are the parameter values that correspond to the

maximum propulsion and hence, will exploit the full potential of a static kite sail for the conditions considered.

The optimal angles of attack, α_{opt} , that lead to maximum kite thrust for different combinations of $U_{z,ref}$ and the ship speed, V , are tabulated in Table 3. It is observed that the numerical model predicts a constant value of 60° for $U_{z,ref} = 20$ m/s. The value of α_{opt} , however, does vary with V at lower reference wind speeds. For $U_{z,ref} = 15$ m/s, the optimal angle of attack decreases with an increase in the ship speed. On the other hand, for $U_{z,ref} = 10$ m/s, the magnitude of the optimal angle of attack first decreases and then increases as the ship speed is increased. It could be confirmed that α_{opt} is more likely to vary for low relative wind speeds, $W_{z,k}$. In fact, for a given wind speed, the maximum deviations of α_{opt} from 60° are observed at the highest ship speed of 7.27 m/s. Despite the variation in α_{opt} , the maximum kite thrust for all combinations is achieved at a high angle of attack. As a result of this variation, the relationship of the parameters with V for different reference wind speeds in the discussion that follows are not entirely due to the effect of $W_{z,k}$, but also due to the different angles of attack.

Table 3. The optimal angles of attack obtained for the different ship and wind speeds considered.

V (m/s)	α_{opt} for $U_{z,ref}=10$ m/s ($^\circ$)	α_{opt} for $U_{z,ref}=15$ m/s ($^\circ$)	α_{opt} for $U_{z,ref}=20$ m/s ($^\circ$)
4.04	59	60	60
4.85	55	60	60
5.66	50	59	60
6.47	60	55	60
7.27	85	54	60

Figure 13 illustrates the kite elevation, z_k , for the optimal angles of attack given in Table 3. The graph shows a decrease in z_k with both an increasing V and a decreasing $U_{z,ref}$ as a result of the reduction in $W_{z,k}$ and hence a reduction in the aerodynamic forces exerted on the static kite. The latter calls for a lower z_t , which is the same reason explained for the effect of wind shear in Section 5.1. Given that α_{opt} remains the same for all values of V with $U_{z,ref} = 20$ m/s, the decrease in z_k with V appears to be consistent. For other points, the variation in α_{opt} comes into effect. The percentage increases in the required z_k vary from 296% to 756% and from 140% to 171% as $U_{z,ref}$ increases from 10 to 15 m/s and from 15 to 20 m/s, respectively. Recalling the positive correlation between z_k and L_k in Figures 7 and 9, these percentages highlight the quadratic relationship between L_k and $W_{z,k}$. If, in operation with $U_{z,ref} = 20$ m/s, the ship speed is reduced from 7.27 to 4.04 m/s for slow steaming, z_k has to be increased from 107 m to 181 m. The latter is well below the 600 m for a pumping kite generator and the 300 m stated for the kites by SkySails in Section 1.

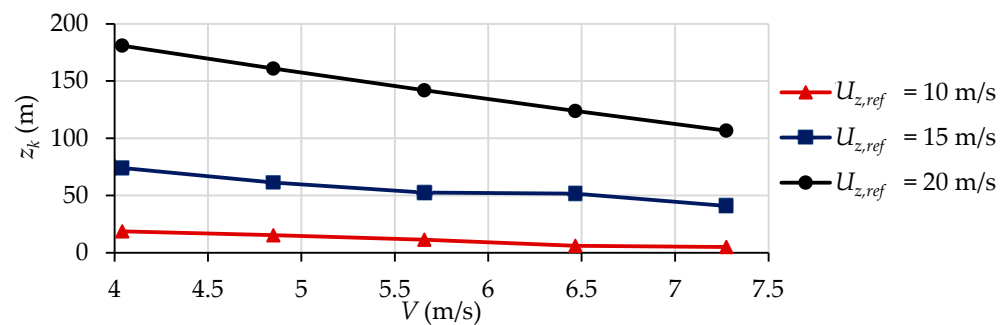


Figure 13. The optimal kite elevations for different ship and wind speeds and a kite area of 320 m².

The dependency on $W_{z,k}$ also applies to the horizontal coordinate of the kite’s COP required for equilibrium. In fact, x_k experiences the same overall decrease discussed for z_k with the exception for $V = 7.27$ m/s and $U_{z,ref} = 10$ m/s, as shown in Figure 14.

Nonetheless, this exception can be attributed to the high α_{opt} for this scenario. In fact, the decrease for the highest wind speed is again uniform. The percentage increases in the case of x_k as $U_{z,ref}$ is increased from 10 to 15 m/s and from 15 to 20 m/s range from 187% to 1105% and from 149% to 230%, respectively, corresponding to higher absolute differences than those for z_k . The values for x_k are higher as well. The maximum x_k of 641 m for a V of 4.04 m/s, $U_{z,ref}$ of 20 m/s and A_k of 320 m² is lower than the limit of about 800 m. The 800 m limit is the limit prescribed from the tether diameter analysis. However, the maximum x_k is 254% higher than the maximum z_k in Figure 13. Hence, the results indicate that for optimal performance, x_k may be of a greater concern than z_k due to the relationship between the two coordinates for high angles of attack.

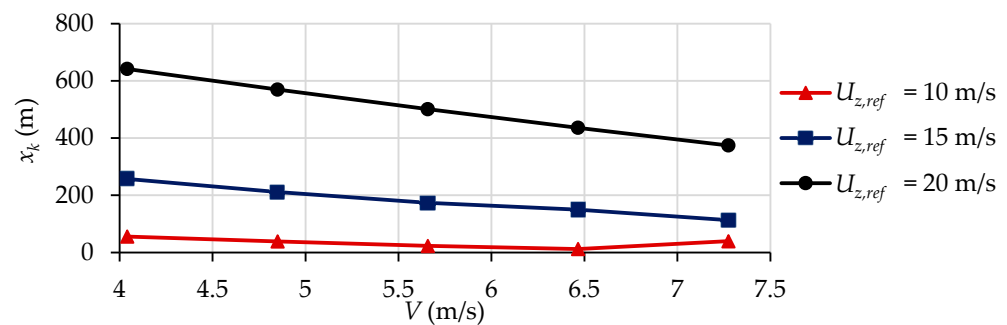


Figure 14. The optimal kite horizontal coordinates for different wind and ship speeds and a kite area of 320 m².

Figure 15 presents the estimated assistance contributed by the kite sail as percentages of the ship resistance at the respective ship speeds. The results correspond to the optimal coordinates in Figures 13 and 14. As expected, the assistance from the kite in overcoming the ship resistance increases with an increasing relative wind speed, either by reducing V or with an increasing $U_{z,ref}$. When the ship travels at the maximum speed with $U_{z,ref} = 10$ m/s, the assistance by the kite is at a negligible value of 0.02%. On the other hand, the ship will be able to accelerate when travelling at $V \leq 4.85$ m/s with $U_{z,ref} = 20$ m/s due to the assistance by the kite being greater than 100%. For this wind speed, the ship can travel at a constant speed of around 5.3 m/s with the kite sail as the only means of propulsion. Considering $V = 5.66$ m/s, the optimal coordinates determined from Figures 13 and 14 are (23.0 m, 11.4 m), (173.5 m, 52.4 m) and (500.9 m, 141.9 m) for the respective $U_{z,ref}$ from 10 to 20 m/s. These coordinates lead to ship propulsion assistance values of 2%, 27% and 79%, respectively. It is shown from Figure 12 that lower ship speeds yield higher proportions of propulsion to originate from the kite. The negative correlation between the ship speed and the propulsion proportions originating from the kite shows the benefits of slow steaming in maximizing the use of WASP systems and reducing the carbon footprint.

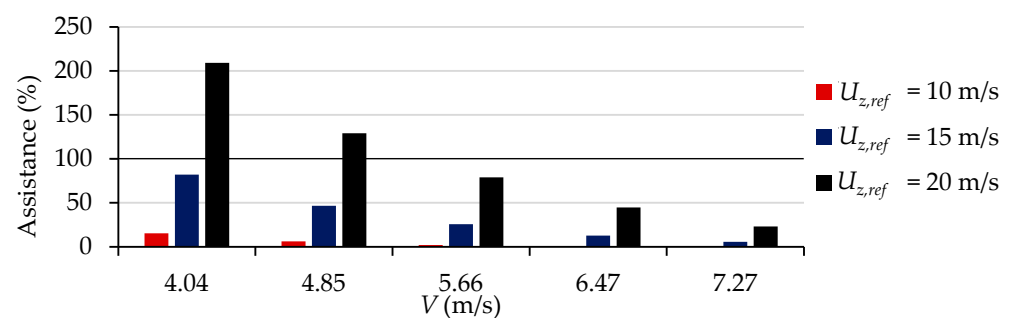


Figure 15. The maximum kite thrust achieved for different wind and ship speeds and a kite area of 320 m² as a percentage of the total ship resistance at the corresponding ship speed.

Figure 16 shows the tether length, l_t , to vary with V and $U_{z,ref}$ similarly to the previously discussed parameters for the wind speed study. The reason is that l_t is effectively a result of the combination of the tether end coordinates, x_t and z_t , based on the path covered by a catenary curve. The two coordinates are functions of the aerodynamic forces as established in Equations (12) and (14) together with the equilibrium analysis in Section 2.5, while the value of z_t has to also satisfy $\Delta z \approx 5$ m. With the aerodynamic forces being functions of $W_{z,k}$, l_t is positively correlated to $W_{z,k}$, thus the positive correlation of l_t to $U_{z,ref}$ and the negative correlation to V . Figure 16 can be compared to Figure 14 to estimate the bridle line lengths that have to be set in order to achieve the values of x_k required for equilibrium conditions. Figure 11 indicates that the aerodynamic forces for a given α have negligible effect on the bridle line lengths. In fact, the greatest discrepancy between x_k and l_t is observed for $V = 7.27$ m/s and $U_{z,ref} = 10$ m/s as a result of the α_{opt} of 85° at which Figure 11 shows the bridle lines to be relatively long. In this scenario, $x_k = 39.5$ m and $l_t = 0.1$ m. Even for the highest wind speed with the ship travelling at 4.04 m/s, l_t required remains within a practical limit of 664 m.

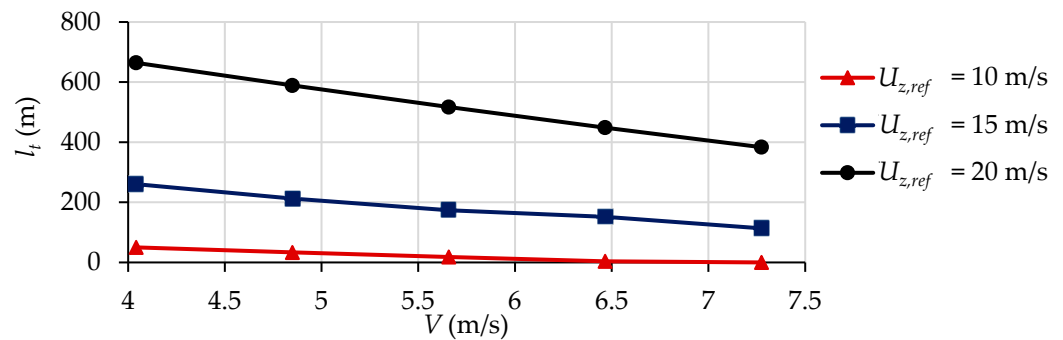


Figure 16. The optimal tether lengths for different wind and ship speeds and a kite area of 320 m².

The variation in the tension at the end of the tether, T_t , with V for optimal performance is depicted for the three reference wind speeds in Figure 17. The value of T_t corresponds to the maximum tension experienced by the tether. Recalling from Section 2.4 that T_t is the resultant of T_H and T_V and that the kite mass is considered negligible such that the latter two tension components are equal to D_k and L_k , respectively, T_t is also equivalent to the resultant aerodynamic force on the kite sail. As a result, T_t is positively correlated to $W_{z,k}$ in the same manner explained for the other parameters in Figures 13–15. Hence, a positive correlation also exists between l_t and T_t , as expected from Equation (15). In fact, T_t is of only 36.0 N when $l_t = 0.1$ m. The maximum value of about 87 kN is again observed for the lowest V and highest $U_{z,ref}$. Nonetheless, it is lower than the safe load of 190 kN for the 42 mm diameter tether and, given that static analysis at the tether end shows T_f and T_r to be lower than T_t , so are the tensions in the bridle lines. The fact that the safe load is not reached suggests that the tether can, in reality, have a smaller diameter. However, the latter will imply an increased tether length to balance the kite lift force with the overall weight of the WASP system, thus increasing x_k and z_k to values that are larger than those presented in Figures 13 and 14.

A smaller diameter will reduce the drag force on the tether. Nonetheless, the estimates presented in Figure 18 indicate that the drag acting on the 42 mm diameter tether, expressed as a percentage of the kite thrust, is only marginal. Therefore, the downward component of the drag that, in practice, would have the same effect of the tether weight, is not likely to influence the kite elevation and propulsive forces. The maximum value obtained at $V = 4.04$ m/s and $U_{z,ref} = 20$ m/s is only of about 1.5%. For a fixed diameter, the tether drag is positively correlated to both the relative wind speed and the elevation of the tether end such that it decreases even further when the ship travels at a higher speed or the wind slows down. For the lowest wind speed with a V of 6.47 and 7.27 m/s, the tether drag is zero because of z_t being so low that the relative wind speed is either zero or in the opposite

direction. With the latter case not being considered in this study, it can be investigated in studies focusing on analysing the forces on the tether in greater detail.

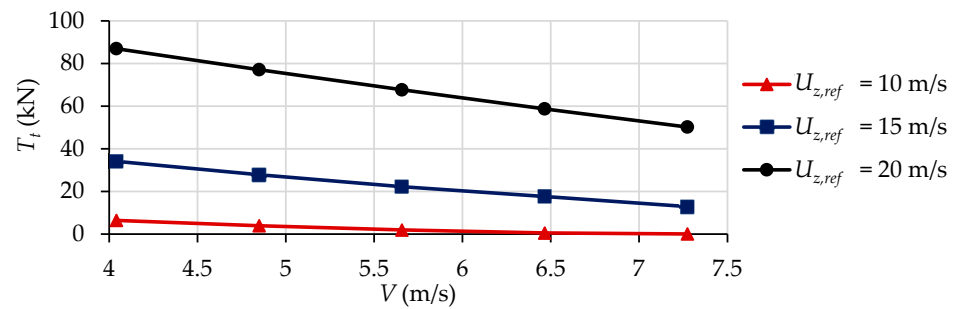


Figure 17. The tether end tensions exhibited with the optimal parameters for different wind and ship speeds and a kite area of 320 m².

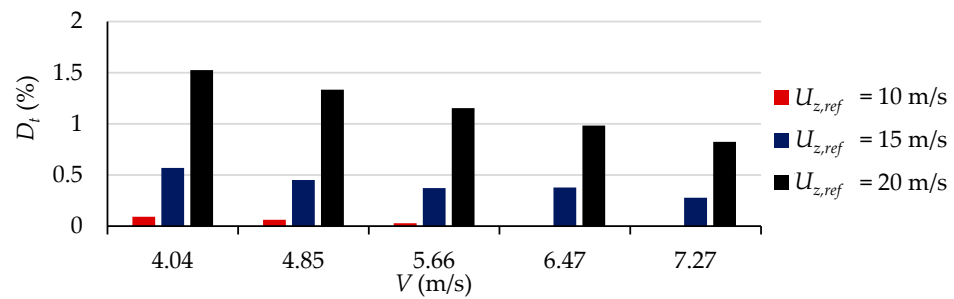


Figure 18. The estimated tether drag for different wind and ship speeds and a kite area of 320 m² as a percentage of the kite thrust for the respective combination of ship and wind speed.

6. Conclusions

The present paper presents the results from a theoretical model investigating the effect of the kite area and the reference wind speed on the performance of a static kite sail used for WASP in the case of a horizontal tail wind. The mathematical formulation is different than those presented in past works. Based on hyperbolic functions of a catenary profile, the model takes into account the weight of the tether and its curvature under the action of its weight to investigate the aerodynamic performance of a static kite sail for any given operating conditions while still maintaining high computational efficiency. In fact, the results show the positive correlation between the kite elevation and the tether length, with the latter having a direct effect on the tether weight. Apart from providing the analysis of the relationships between the different parameters of importance to kite operation for WASP applications and the achievable power outputs for the considered input parameters, this paper presents a new computationally efficient model that can be applied to different operating conditions as well as different types of ships, tethers and kite sails. Hence, the model can be used to determine the best combination of dimensions and materials that lead to the greatest reduction in the carbon footprint from the maritime sector. Important conclusions from this study include the following:

- The correlations between the aerodynamic forces and output parameters that determine the performance of the kite sail are generally positive.
- The effect of the kite area varies with the angle of attack given that wind shear also comes into effect when the kite elevation has to be changed in response to a different lift force. In fact, doubling the kite area for an angle of attack of 60° increases the kite thrust by about 150%.
- The kite coordinates corresponding to the maximum propulsive drag were found to satisfy practical limits for all the ship and tail wind speeds considered.
- For the highest reference wind speed of 20 m/s, about 80% of the required propulsion can be provided by the kite sail if the 75 m long Series 60 vessel travels at a speed of

5.66 m/s with a tail wind while the angle of attack and coordinates of the kite are set to 60° and (500.9 m, 141.9 m), respectively.

- The modelled ship can be propelled solely by the 320 m² static kite sail at a speed of about 5.3 m/s when the wind speed is 20 m/s at a height of 90 m. At this wind speed of 20 m/s, the optimal angle of attack leading to maximum thrust was also found to be constant at a value of 60° for all ship speeds considered. However, the optimal angle of attack is expected to vary for low relative wind speeds.
- The safe load of 190 kN set for the tether was never reached in the scenarios considered. Additionally, the maximum tether drag as a percentage of the kite thrust as estimated in this study for maximum thrust conditions was found to be only of about 1.5%.

The study presented in this paper also highlights the benefits of slow steaming given the observed increase in propulsion assistance for lower ship speeds.

The kite sail in this study is approximated to a flat finite wing. Hence, future work should consider further analysis of the aerodynamics of the kite sail, using more comprehensive modelling by means of CFD, while also taking into account the curvature of the sail and the Reynolds Number effects. The influences of unsteady aerodynamics resulting from intermittent wind conditions, such as dynamic stall, should also be investigated. Further work should evaluate the reliability of existing dynamic stall models, originally developed for aircraft and wind turbine rotor applications, when modelling the transient aerodynamic loads experienced by kites in WASP applications. Given that this paper only provides a theoretical assessment of the static kite sail, validation of the proposed numerical model using experiments on a WASP prototype operating under open sea conditions is recommended for future work. Further work should also consider the influence of the misalignment between the wind and the ship route. Such consideration is also crucial for application of the presented model in dynamic kite flight.

Author Contributions: Conceptualisation, W.F., T.S. and C.D.M.M.-F.; methodology, W.F., T.S. and C.D.M.M.-F.; software, W.F., T.S. and C.D.M.M.-F.; validation, W.F., T.S. and C.D.M.M.-F.; formal analysis, W.F., T.S. and C.D.M.M.-F.; investigation, W.F., T.S. and C.D.M.M.-F.; writing—original draft preparation, W.F.; writing—review and editing, W.F., T.S., C.D.M.M.-F. and M.F.; visualisation, T.S. and C.D.M.M.-F.; supervision, T.S. and C.D.M.M.-F.; project administration, T.S. and C.D.M.M.-F.; funding acquisition, T.S. and C.D.M.M.-F. All authors have read and agreed to the published version of the manuscript.

Funding: The presented work has been supported through the collaborative programme of the VENTuRE (project no. 856887) EU-funded H2020 project.

Institutional Review Board Statement: Not applicable.

Data Availability Statement: Not applicable.

Conflicts of Interest: The authors declare no conflict of interest. The funders had no role in the design of the study; in the collection, analyses, or interpretation of data; in the writing of the manuscript; or in the decision to publish the results.

Nomenclature

CFD	Computational Fluid Dynamics
COP	Centre of pressure
WASP	Wind-assisted ship propulsion
c_d	Drag coefficient of a two-dimensional aerofoil (-)
c_l	Lift coefficient of a two-dimensional aerofoil (-)
c_m	Moment coefficient of a two-dimensional aerofoil (-)
c_{ref}	Reference chord of a finite wing at the midspan (m)
d_t	Tether diameter (m)
l_f	Front bridle line length (m)
l_r	Rear bridle line length (m)
l_t	Tether length (m)

x_k	Horizontal coordinate of the kite's centre of pressure (m)
x_t	Horizontal coordinate of the tether end (m)
z	A given elevation above the mean seawater level (m)
z_0	Surface roughness length of the seawater (m)
z_k	Kite elevation (m)
z_{ref}	Reference height at which the wind speed is known (m)
z_s	Elevation above sea surface at which the relative wind speed is zero (m)
z_t	Elevation of the tether end (m)
A_k	Area of the elliptical kite planform (m ²)
AR	Aspect ratio of the elliptical kite planform (-)
B	Ship beam (m)
C_B	Ship block coefficient (-)
C_D	Drag coefficient of a finite wing (-)
$C_{D,i}$	Induced drag coefficient of a finite wing (-)
$C_{D,t}$	Tether drag coefficient (-)
C_L	Lift coefficient of a finite wing (-)
D_k	Drag force on a finite wing (N)
D_t	Tether drag (N)
L	Ship length (m)
LCB	Longitudinal centre of buoyancy (%L)
L_f	Ship length in feet (ft)
L_k	Lift force on a finite wing (N)
P_E	Naked effective power of a ship (kW)
R_{air}	Air resistance on a ship (N)
R_{App}	Appendage resistance of a ship (N)
R_{Eff}	Effective ship resistance (N)
R_{Naked}	Naked hull resistance (N)
R_{PM}	Ship resistance due to the power margin (N)
R_T	Total ship resistance (N)
T	Ship draught (m)
T_f	Front bridle line tension (N)
T_H	Horizontal component of the tether end tension (N)
T_V	Vertical component of the tether end tension (N)
T_r	Rear bridle line tension (N)
T_t	Tether end tension (N)
$U_{z,k}$	True wind speed at the kite elevation (m/s)
$U_{z,ref}$	True wind speed at the reference height (m/s)
V	Ship speed (m/s)
V_k	Ship speed in knots (kn)
W_z	Relative wind speed at a given elevation (m/s)
$W_{z,k}$	Relative wind speed at the kite elevation (m/s)
s	Corrected ship resistance coefficient (-)
α	Kite angle of attack (°)
α_{opt}	Kite optimal angle of attack (°)
β	Angle of the rear bridle line with the horizontal (°)
Δ	Ship load displacement (t)
Δz	Vertical distance between the tether end and the kite's centre of pressure (m)
ζ	Angle of the front bridle line with the horizontal (°)
μ_t	Tether weight per unit length (N/m)
ρ_a	Air density (kg/m ³)
ρ_w	Water density (kg/m ³)

References

1. Brooks, M.R.; Faust, P. Review of Maritime Transport—A historical Perspective. In *50 Years of Review of Maritime Transport, 1968–2018: Reflecting on the Past, Exploring the Future*; United Nations Conference on Trade and Development: Geneva, Switzerland, 2018; pp. 3–36.
2. Maritime Shipping—International Council on Clean Transportation. Available online: <https://theicct.org/sector/maritime-shipping/> (accessed on 10 November 2022).

3. Estimates of carbon intensity. In *Fourth IMO GHG Study 2020 Full Report*; International Maritime Organisation: London, UK, 2021; pp. 167–216.
4. Brooks, M.R.; Faust, P. *Invited Essays and Reflections by Distinguished Persons. In 50 Years of Review of Maritime Transport, 1968–2018: Reflecting on the Past, Exploring the Future*; United Nations Conference on Trade and Development: Geneva, Switzerland, 2018; pp. 37–54.
5. Chou, T.; Kosmas, V.; Acciaro, M.; Renken, K. A Comeback of Wind Power in Shipping: An Economic and Operational Review on the Wind-Assisted Ship Propulsion Technology. *Sustainability* **2021**, *13*, 1880. [CrossRef]
6. Degiuli, N.; Martić, I.; Farkas, A.; Gospić, I. The impact of slow steaming on reducing CO₂ emissions in the Mediterranean Sea. *Energy Rep.* **2021**, *7*, 8131–8141. [CrossRef]
7. Traut, M.; Gilbert, P.; Walsh, C.; Bows, A.; Filippone, A.; Stansby, P.; Wood, R. Propulsive power contribution of a kite and a Flettner rotor on selected shipping routes. *Appl. Energy* **2014**, *113*, 362–372. [CrossRef]
8. Leloup, R.; Roncin, K.; Bles, G.; Leroux, J.-B.; Jochum, C.; Parlier, Y. Kite and classical rig sailing performance comparison on a one design keel boat. *Ocean Eng.* **2014**, *90*, 39–48. [CrossRef]
9. Leloup, R.; Roncin, K.; Behrel, M.; Bles, G.; Leroux, J.-B.; Jochum, C.; Parlier, Y. A continuous and analytical modeling for kites as auxiliary propulsion devoted to merchant ships, including fuel saving estimation. *Renew. Energy* **2016**, *86*, 483–496. [CrossRef]
10. Bigi, N.; Roncin, K.; Leroux, J.-B.; Parlier, Y. Ship Towed by Kite: Investigation of the Dynamic Coupling. *J. Mar. Sci. Eng.* **2020**, *8*, 486. [CrossRef]
11. Clodic, G.; Gilloteaux, J.C.; Babarit, A. Wind propulsion options for energy ships. In Proceedings of the 1st ASME International Offshore Wind Technical Conference, San Francisco, CA, USA, 4 November 2018. [CrossRef]
12. Technology SkySails Yacht. Available online: <https://skysails-yacht.com/technology.html> (accessed on 11 November 2022).
13. Fechner, U.; van der Vlugt, R.; Schreuder, E.; Schmehl, R. Dynamic model of a pumping kite power system. *Renew. Energy* **2015**, *83*, 705–716. [CrossRef]
14. Products SkySails Yacht. Available online: <https://skysails-yacht.com/products.html> (accessed on 11 November 2022).
15. SkySails and Humphreys Yacht Design Present Towing Kite Propulsion for Superyachts. Available online: <https://www.superyachttimes.com/yacht-news/skysails-and-humphreys-yacht-design-present-towing-kite-propulsion-for-superyachts> (accessed on 12 November 2022).
16. MS Beluga SkySails—Cargo Ship. Available online: <https://www.ship-technology.com/projects/msbelugaskysails/> (accessed on 11 November 2022).
17. German High-Tech Sky Sail May Cut Costs, Emissions. Available online: <https://www.reuters.com/article/us-germany-sails-idUSL2947265420061204> (accessed on 11 November 2022).
18. Molland, A.F.; Turnock, S.R.; Hudson, D.A. Propulsive Power. In *Ship Resistance and Propulsion*, 1st ed.; Cambridge University Press: Cambridge, UK, 2011; pp. 7–11.
19. Sabit, A.S. An analysis of the Series 60 results: Part I, Analysis of forms and resistance results. *Int. Shipbuild. Prog.* **1972**, *19*, 81–97. [CrossRef]
20. Molland, A.F.; Turnock, S.R.; Hudson, D.A. Resistance Design Data. In *Ship Resistance and Propulsion*, 1st ed.; Cambridge University Press: Cambridge, UK, 2011; pp. 188–245.
21. Molland, A.F.; Turnock, S.R.; Hudson, D.A. Hull Form Design. In *Ship Resistance and Propulsion*, 1st ed.; Cambridge University Press: Cambridge, UK, 2011; pp. 313–336.
22. Molland, A.F.; Turnock, S.R.; Hudson, D.A. Components of Hull Resistance. In *Ship Resistance and Propulsion*, 1st ed.; Cambridge University Press: Cambridge, UK, 2011; pp. 12–68.
23. Davis, G. Resistance and Powering of Ships. In *EN400 Principles of Ship Performance Course Notes*; United States Naval Academy: Annapolis, MD, USA, 2014; pp. 7.1–7.46.
24. Manwell, J.F.; McGowan, J.; Rogers, A.L. Wind Characteristics and Resources. In *Wind Energy Explained: Theory, Design and Application*, 2nd ed.; John Wiley and Sons: Hoboken, NJ, USA, 2009; pp. 23–90.
25. Anderson, J.D. Incompressible Flow over Airfoils. In *Fundamentals of Aerodynamics*, 6th ed.; McGraw-Hill Education: New York, NY, USA, 2017; pp. 321–422.
26. Leishman, J.G.; Beddoes, T.S. A Semi-Empirical model for dynamic stall. *J. Am. Helicopter Soc.* **1989**, *34*, 3–17. [CrossRef]
27. Larsen, J.W.; Nielsen, S.R.; Krenk, S. Dynamic stall model for wind turbine airfoils. *J. Fluids Struct.* **2007**, *23*, 959–982. [CrossRef]
28. GBangga, G.; Lutz, T.; Arnold, M. An improved second-order dynamic stall model for wind turbine airfoils. *Wind Energy Sci.* **2020**, *5*, 1037–1058. [CrossRef]
29. Snel, H. Heuristic modelling of dynamic stall characteristic. In Proceedings of the European Wind Energy Conference, Dublin, Ireland, 6 October 1997.
30. Molland, A.F.; Turnock, S.R. Physics of control surface operation. In *Marine Rudders and Control Surfaces*, 1st ed.; Butterworth-Heinemann: Oxford, UK, 2007; pp. 21–56.
31. Houghton, E.L.; Carpenter, P.W. Finite Wing Theory. In *Aerodynamics for Engineering Students*, 5th ed.; Butterworth-Heinemann: Oxford, UK, 2003; pp. 210–272.
32. Meriam, J.L.; Kraige, L.G.; Bolton, J.N. Distributed Forces. In *Engineering Mechanics: Statics*, 8th ed.; John Wiley and Sons: Hoboken, NJ, USA, 2016; pp. 229–330.
33. White, F.M. Flow Past Immersed Bodies. In *Fluid Mechanics*, 7th ed.; McGraw-Hill: New York, NY, USA, 2011; pp. 457–528.

34. Sheldahl, R.E.; Klimas, P.C. *Aerodynamic Characteristics of Seven Symmetrical Aerofoil Sections Through 180-Degree Angle of Attack for Use in Aerodynamic Analysis of Vertical Axis Wind Turbines*; Sandia National Laboratories: Albuquerque, NM, USA, 1981; pp. 27–40.
35. Resistance and Power Requirements Calculated for Any MAXSURF Design. Available online: <https://maxsurf.net/resistance-and-power-requirements> (accessed on 14 November 2022).
36. Wire Rope—Strength. Available online: https://www.engineeringtoolbox.com/wire-rope-strength-d_1518.html (accessed on 18 August 2022).

Disclaimer/Publisher’s Note: The statements, opinions and data contained in all publications are solely those of the individual author(s) and contributor(s) and not of MDPI and/or the editor(s). MDPI and/or the editor(s) disclaim responsibility for any injury to people or property resulting from any ideas, methods, instructions or products referred to in the content.